Available online at www.sciencedirect.com
ScienceDirect
Trans. Nonferrous Met. Soc. China 33(2023) 2943−2954
Transactions of Nonferrous Metals Society of China
www.tnmsc.cn

Atomic-level insights on enhanced strength and ductility of Al−Mg−Si alloys with β''-Mg_5Si_6 at cryogenic temperatures

Gang LEI[1,2], Hai-tao GAO[1,2,3], Yun ZHANG[1,2], Xiao-hui CUI[1,2,3], Hai-liang YU[1,2,3]

1. School of Mechanical and Electrical Engineering, Central South University, Changsha 410083, China;
2. State Key Laboratory of Precision Manufacturing for Extreme Service Performance, Central South University, Changsha 410083, China;
3. Light Alloy Research Institute, Central South University, Changsha 410083, China

Received 1 May 2022; accepted 26 August 2022

Abstract: The influences of β'' phase volume fractions (PVF) and cryogenic temperatures on nanomechanical properties of Al−Mg−Si alloys were simulated by molecular dynamics. The simulation results show that when the β'' PVF is 0.107 at 77 K, the peak stress of Al−Mg−Si alloy is increased by 97.05% compared to that of pure aluminum. When the β'' PVF is 0.107, the peak stress of the sample at 27 K is increased by up to 23.55% compared to peak stress of sample at 300 K. Cryogenic environments help to enhance total dislocation density, allowing samples to withstand greater stress, which can provide additional strength and ductility. Temperature decrease can also appreciably inhibit the initiation and growth of voids (growth rate is decreased by 88.5% at 27 K), which contributes to the enhanced ductility.

Key words: molecular dynamics; aluminum alloy; β'' phase; strength; ductility; cryogenic temperature

---

1 Introduction

Due to desirable properties such as high specific strength, good formability, and excellent corrosion resistance, aluminum alloys are widely used in the engineering field [1−3]. A typical example is the strengthening of the age hardenable Al−Mg−Si alloys by a series of metastable precipitates under peak aging, leading to peak hardness. Therein, the fully coherent needle-shape β'' phase is the main strengthening phase [4,5]. The generally accepted precipitation sequence in Al−Mg−Si alloys is [6−8]: SSSS→$(Mg+Si)_{\text{clusters}}$→ pre-$\beta''$/GP-$I_{\text{spherical}}$→$\beta''$/GP-$II_{\text{needle-shape}}$→$\beta'$, B′ (Mg/Si>1); U1, U2 (Mg/Si≤1)→β(+Si), where SSSS represents a super-saturated solid solution, GP denotes Guinier−Preston zones. Except for the β phase, other precipitate phases are metastable during aging [9]. Thermodynamically metastable phases are nonequilibrium and unstable, and therefore it is difficult to prepare and measure their mechanical properties experimentally. However, it is vital to reveal the effect of precipitates on properties in Al−Mg−Si alloys for alloy designs and novel processes developments.

The strength and hardness of Al−Mg−Si alloys mainly depend on the phase volume fraction (PVF); meanwhile, these property parameters are further influenced by processing conditions. Enhanced strength and ductility of metallic materials are often mutually constrained because the ductility generally decreases with increasing strength [10,11]. A typical example is the high-strength nanocrystalline (NC) metal with a grain size of less than 100 nm, which has a major drawback of low ductility (5%−8%). Therefore, the deserved importance as structural material of NC metals is limited. To solve

---

Corresponding author: Hai-liang YU, Tel/Fax: +86-18511635397, E-mail: yuhailiang@csu.edu.cn, yuhailiang1980@tom.com;
Hai-tao GAO, E-mail: gaohaitao@csu.edu.cn

DOI: 10.1016/S1003-6326(23)66309-5

the problem, cryo-forming techniques [12−15] are becoming attractive in scientific research and engineering application. Improved yield strength and ductility of commercial Al−Mg−Si alloys by cryorolling [12,13], the preparation of high-strength and high-ductility nanostructural AA1050 using asymmetric cryorolling [14], and improvement of tensile strength in AA6061 by cryorolling + warm rolling + peak aging [15]. Recently, the AA6061 shows higher tensile strength and ductility in cryogenic environment compared to room temperature via experimental study [16]. The ultimate tensile strength and elongation of AA6061 at 173 K can be enhanced by up to about 15% and 50%, respectively. Such a trend may be ascribed to the fact that greater diffusion and entanglement of the dislocations may occur at cryogenic temperature [11,17,18]. However, it is still unclear how the Al−Mg−Si alloy system containing the β'' phase would respond to cryogenic temperature changes and what the underlying physical mechanisms are, especially the strength and ductility synergistic- increase effect of Al−Mg−Si alloy in cryogenic environment.

To reveal the relationships between mechanical responses and physical conditions, numerous researches on characterization and computation have been performed using molecular dynamics (MD) simulations. YUAN et al [19] investigated the tensile response behaviors of single-crystal Al nanowires at different temperatures and strain rates. ZEPEDA-RUIZ et al [20] utilized atomic simulations to quantify the conditions under which the limits of dislocation-mediated plasticity are reached in metal tantalum, and to predict cheaply the deformation twinning when tantalum is beyond any such limit. The dislocation activity of metal crystals can refer to the recent simulation work of KO et al [21]. After generating preexisting dislocations, they found that the total yield and flow stress were controlled by the longest mobile dislocations in relatively large Cu crystals with abundant initial mobile dislocations. And the solid−solid phase transition problem in metals can be studied by MD [22]. Nevertheless, there are few reports on the nanomechanical properties and temperature effect on the Al−Mg−Si alloy system containing the β'' phase. But these properties are crucial for the development of novel alloys and processes and going to be calculated by MD in this work.

In this study, Al matrix+β'' phase was chosen to investigate the enhanced strength and ductility at cryogenic temperature. The model was three-dimensional so that β'' phase was completely constrained by the Al matrix. The structure of β'' needle-shape precipitate is monoclinic [4] with a space group of $C2/m$, and its stoichiometry is generally considered to be Mg_5Si_6, according to that experimentally measured by ZANDBERGEN et al [23]. Although the stoichiometry of β'' phase may be more complex in further realistic observations, ranging from Al-rich configuration (β''-$Mg_4Al_3Si_4$) to Al-free configuration (β''-Mg_5Si_6 and β''-Mg_7Si_4), for simplicity, β''-Mg_5Si_6 was selected as the atomic structure of precipitate and MD simulations were employed to get further observations about the nanomechanics of the model with β''-Mg_5Si_6, including temperature effect.

2 Simulation model and method

The crystal structure information of the Al matrix and β'' phase (listed in Table 1) and their orientation relationships were determined before modeling. Previous works [9,26] indicated that the relationships of Al/β'' were:

$$[230]_{\mathrm{Al}} // [100]_{\beta''}^{\mathrm{Conv.}},\ [001]_{\mathrm{Al}} // [010]_{\beta''}^{\mathrm{Conv.}},\ [\bar{3}10]_{\mathrm{Al}} // [001]_{\beta''}^{\mathrm{Conv.}} \quad (1)$$

where the superscript "Conv." in Eq. (1) represents β'' conventional cell. However, the orientation

Table 1 Crystal structure information of Al matrix and β'' phase

Component	Structure	Lattice parameter				Source
		a/nm	b/nm	c/nm	β/(°)	
β'' phase	Monoclinic ($C2/m$)	1.589	0.394	0.657	103.3	This work [24]
		1.583	0.398	0.652	105	Theoretical [25]
		1.516	0.405	0.674	105.3	Experimental [23]
Al matrix	FCC	0.405	−	−	−	

indexes of the Al matrix in this work need to be orthogonal, the *z*-direction was set to be $[\bar{3}20]$ and the *y*-direction to be $[00\bar{1}]$ [27]. The third term in Eq. (1) is still satisfied at the moment. Thus, the orientation indexes of the Al matrix are given by

$$O=x[230],\ y[00\bar{1}],\ z[\bar{3}20] \tag{2}$$

An FCC single-crystal Al nanowire (see Fig. 1) with a volume of 15 nm × 45 nm × 15 nm (the lattice constant a_{Al} of Al matrix was set as 0.405 nm, as shown in Table 1) was prepared according to the orientation index in Eq. (2). Then, the β'' conventional cell was expanded by 5 and 12 times along $a_{\beta''}$ and $c_{\beta''}$ directions, respectively. The β'' length along $b_{\beta''}$ direction (that is the growth direction of β'' phase) was a control variable l_b, the volume of β'' supercell equals $7.95\times l_b\times 7.89\times \sin\beta$ nm^3, therein β=103.3°. The β'' supercell was embedded into the Al matrix generated in the first step, and finally, the Al atoms overlapping with the β'' supercell were deleted. So the initial configuration of the Al−Mg−Si alloy sandwich structure model was established, and the β'' phase volume fraction (PVF, φ) $\varphi=7.95\times l_b\times 7.89\times \sin\beta/(15\times 45\times 15)=6.029\times 10^{-3}\, l_b$. Despite the β'' PVF changing atom number *N*, the *N* always fluctuated around 600000 with a small deviation. As for the atomic interaction, the modified embedded-atom method (MEAM) potential for Al, Si, and Mg, etc [28] was employed. Recently, the potential has been widely used in the studies of mechanical properties and strengthening mechanisms of Al and Mg alloys [29−33].

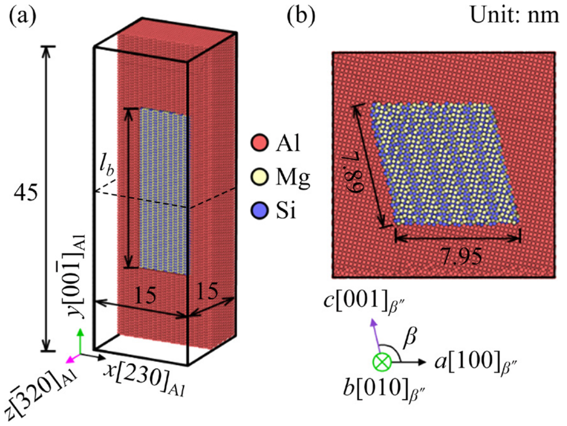

Fig. 1 Al−Mg−Si alloy sandwich structure model: (a) Size and orientation index of Al matrix (longitudinal-section diagram); (b) Configuration and relationship with Al matrix of β'' phase (cross-section diagram), which is top view of (a) after slicing along dashed line (The β'' phase is monoclinic, $\alpha=\gamma$=90°, but β=103.3°, so the cross-section of the β'' phase in (b) is a parallelogram)

Two kinds of schedules were performed in this work as shown in Table 2. (1) The default value of simulation temperature was set to be 77 K, and the β'' PVFs were changed to investigate the mechanical properties of Al−Mg−Si alloy samples. (2) According to the simulation results in the Schedule (1), the sample had best performances at φ=0.107, and thus the default of β'' PVF was set to be 0.107 when the temperature decreased from 300 to 27 K.

Table 2 Simulation parameters for Al−Mg−Si alloy samples

Parameter	Value	Default
β'' length, l_b/nm	0, 5.9, 11.8, 17.7, 23.6, 29.5	17.7
β'' volume/nm^3	0, 360.2, 720.3, 1080.5, 1440.6, 1800.8	1080.5
β'' PVF, φ	0, 0.036, 0.071, 0.107, 0.142, 0.178	0.107
Temperature/K	27, 77, 127, 177, 227, 300	77

l_b and φ=0 represent the Al matrix without β'' phase. The β'' volume of 12−2100 nm^3 was measured in Ref. [34], and the volume in this work was within the range. As for tensile temperature, 300 and 77 K were widely used in the experiments, and four other temperatures were taken with equal intervals as far as possible, so the tensile temperature levels were 27, 77, 127, 177, and 300 K

The geometric modeling and numerical solution in this work were implemented using LAMMPS [35]. The *y*-direction uniaxial tensile simulations were performed using the velocity−Verlet integration algorithm at a time step of 1 fs (=1×10^{-15} s) and a strain rate of 1×10^{9} s^{-1}. Before uniaxial stretching, the samples were firstly optimized by Polak−Ribiere version of the conjugate gradient algorithm to the potential energy minimization state. Then, the temperature was lowered from the initial temperature of 300 K to the target temperature (see Table 2), followed by a relaxation of 150 ps to the equilibrium state. The above two steps were carried out in the isothermal−isobaric ensemble under periodic boundary conditions in three directions. After that, the tension was executed in the Nosé−Hoover thermostat for constant temperature, at which the *x*-direction was changed to a free boundary to observe the necking. The Open Visualization Tool (OVITO) [36] provides post-processing capabilities to visualize the stretching and deformation of the samples and to obtain snapshots at different moments. The OVITO also allows the analysis and visualization of the von Mises stress (calculated by LAMMPS) on each atom, and the atomic strain localization on the y-axis. Furthermore, dislocation extraction algorithm (DXA) [37,38] was used to identify the microstructure type and to analyze in detail the type and density of dislocation extracted.

3 Results and discussion

3.1 Effect of β'' PVF (φ) on nanomechanical properties of Al−Mg−Si samples at cryogenic temperatures

The tensile curves and the variation patterns of peak and flow stress are shown in Fig. 2. The uniaxial tensile curves of all samples are very similar to the common engineering stress−strain curves (see Fig. 2(a)). In the beginning, the engineering stress increases monotonically with the strain. After reaching the peak, a sudden drop occurs. Moreover, the slope of the tensile curves of the samples containing β'' is significantly greater than that of pure Al at a small engineering strain ε (<0.045). Notably, the tensile response of the sample in this work differs from that of the polycrystalline containing many grain boundaries, so that the abrupt drop of tensile curve is not yielding but rather a certain scale of dislocations in the single-crystal, as compared with the experimental tensile curve [39]. According to the tensile curves in Fig. 2(a), the elastic modulus of samples with different β'' PVFs was calculated and listed in Table 3. For β'' PVF φ=0.107, the elastic modulus is the highest and 75.58% higher than that of pure aluminum (β'' PVF φ=0).

Table 3 Elastic modulus of samples

β'' PVF, φ	Elastic modulus/GPa
0	53.36
0.036	80.64
0.071	92.32
0.107	93.69
0.142	89.01
0.178	92.18

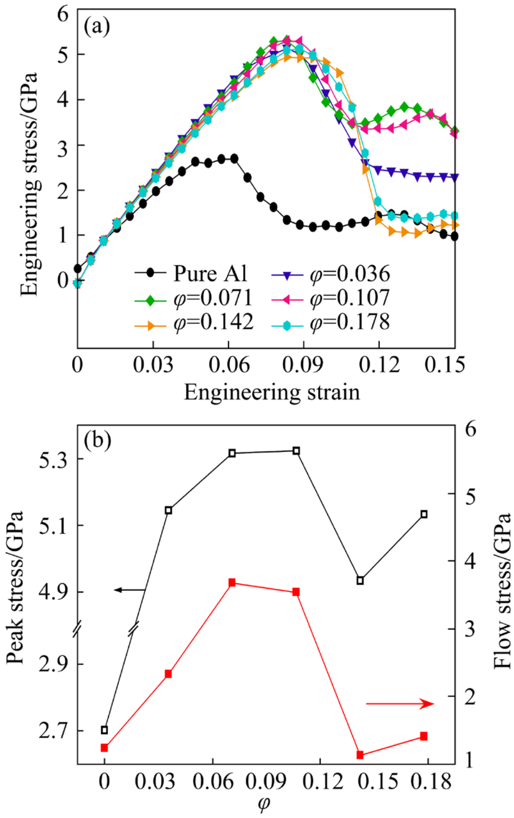

Fig. 2 Uniaxial tensile curves of Al−Mg−Si alloy with different β'' PVF (a), and peak stress and flow stress change over β'' PVF (b)

In Fig. 2(a), the main reason for the primary peak in the engineering stress−strain curve is the nucleation and propagation of dislocations, which pass through the perfect FCC lattice and leave stacking faults in the sample. After the stacking faults accumulate to a certain level, the strain due to dislocation motion exceeds the applied strain and the stress reaches a primary peak and then decreases to allow subsequent dislocation motion. For some samples such as the β'' PVF φ=0, 0.071, and 0.107, there are two stress peaks on the curves, and the secondary peaks present a rise and fall in stress. In the atomic simulation, when the dislocations undergo annihilation and nucleation, the tensile stress oscillates.

Figure 2(b) shows that there has been an obvious upgrade of the nanomechanical properties due to the existence of β'' phase. In this work, peak stress is used to evaluate the tensile strength of the sample. The higher the peak stress is, the higher the tensile strength is. The engineering stress peaks at φ=0.107, where the peak stress increases by 97.05% (note that the samples are ideal single-crystal models, so it is not so high in realistic observations) compared to the pure Al sample. Therefore, there is a great strengthening for the samples with β'' phase in tensile direction (also the growth direction of β'' phase). Meanwhile, the peak and flow stresses at φ=0.071 and 0.107 are higher than those of other samples. As for flow stress, it can be understood that the true stress is required to produce a certain instantaneous plastic flow after the peak stress, which is the second evaluation index. They both show an increasing and then decreasing trend, but the peak of flow stress appears at φ=0.071, which indicates that a larger external stress is required to continue the transient deformation in the late tensile stage (ε>0.12). To sum up, it is complicated how the β'' PVF affects the tensile mechanical properties in the y-direction, so the nanomechanical behaviors are analyzed further to gain atomistic insights into the transition caused by the changes of β'' PVF.

The atomic strain distribution can visualize the areas of severe deformation within samples during stretching, so it is natural to calculate the degree of strain localization on the y-axis and compare the differences from the changes in β'' PVF. The degree of strain localization (Fig. 3(a)) for samples with different β'' PVF is calculated using the parameter ψ defined by CHENG et al [40]:

$$\psi=\sqrt{\frac{1}{N}\sum_{i=1}^{N}\left(\varepsilon_i^{\text{Atomic}}-\varepsilon_{\text{ave}}^{\text{Atomic}}\right)^2} \tag{3}$$

where N is total number of atoms, $\varepsilon_i^{\text{Atomic}}$ is the atomic strain of the ith atom, and $\varepsilon_{\text{ave}}^{\text{Atomic}}$ is average atomic strain of samples. The larger the ψ, the greater the tendency to show a wider strain distribution range of atoms, which laterally reflects the presence of a larger local strain maximum (see Fig. 3(b)).

In Fig. 3(a), none of these five Al−Mg−Si alloy sandwich samples containing the β'' phase undergoes atomic strain localization when the engineering strain ε is zero. Upon further deformation, slow growth occurs in the degree of atomic strain localization within all five samples until ε=0.09. When ε>0.09, the sample with φ=0.036 begins to show larger atomic strain localization firstly, and its final localization degree is larger than that of the samples with φ=0.071 and 0.107. However, the localization degree of the latter two samples increases steadily with deformation. At ε=0.105, the localization degrees with φ=0.142 and 0.178 begin to increase sharply and at a much higher rate than those of previous three samples, and their final strain localization degrees also rank among the highest and second-highest, respectively. It is also worth mentioning that the reason for dramatic transition in the localization degree (namely φ=0.107 and 0.142) comes from a slight change in the β'' PVF (and the β'' phase length l_b differs by only 5.9 nm), which indicates that a small change in the configuration of Al matrix coupled with β'' phase can also cause a large response during deformation.

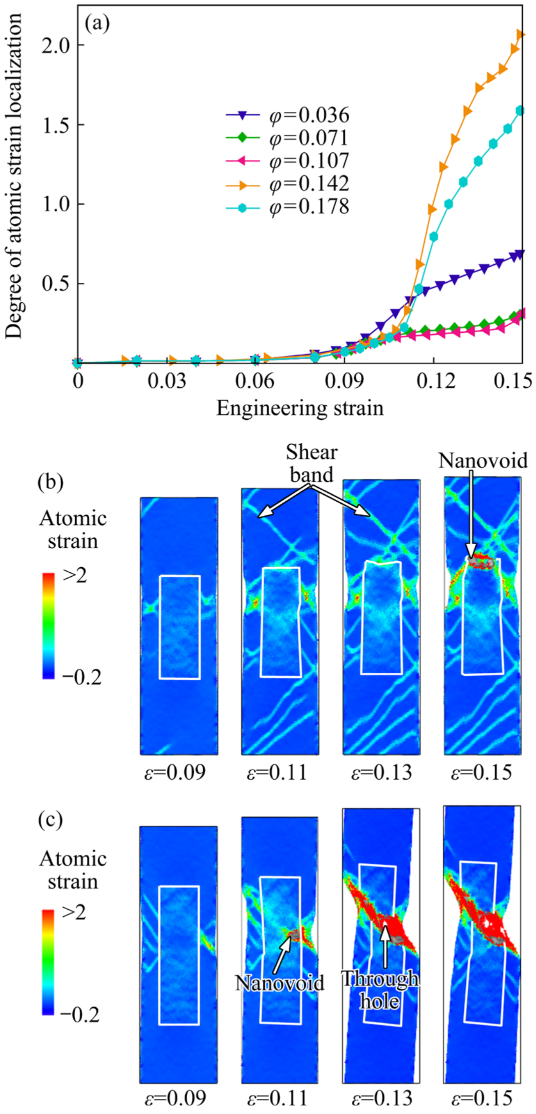

Fig. 3 Degree of atomic strain localization at cryogenic temperature (a), distribution of atomic strain at φ=0.107 (b), and growth of through hole at φ=0.142 (c)

The atomic strain distributions of the samples with φ=0.107 and 0.142 are shown in Fig. 3(b, c), respectively, which reveals a great difference between the two samples for the same engineering strain ε. The profile of the β'' phase is marked with a white wireframe, and the variation of the area surrounded by the white line can reflect the deformation of the β'' phase. Figure 3(c) also shows some important defects in the samples during the stretching, such as nanovoids and through holes, which are also reported in the relevant MD simulation [41]. Notably, even in the z-direction with the periodic boundary condition, the nanovoids develop into through holes when the simulation is not yet finished (ε=0.13, Fig. 3(c)). In such cases, the local deformation of the sample with φ=0.142 is quite drastic, corresponding to the results in Fig. 2(b).

The higher resistance to deformation for the sample with φ=0.107 may be because shear bands "avoid" the β'' phase and distribute at the upper and lower ends of the Al matrix. Meanwhile, the local accumulation of atoms at the Al/β'' interface allows only a small amount of necking. When ε=0.11, the sample with φ=0.142 also starts to form local defects at almost the same position on the right side, as the sample with φ=0.107. However, these nanovoid defects are closer to the waist of β'' phase with relatively high atomic strain, leading to a fatal result. That is to say, a nearly 45° shear band along the x-direction cuts almost through the entire sample from the waist, including the β'' phase as well. However, the rest regions of the Al matrix hardly show the same landscapes as in the sample with φ=0.107.

Next, the dislocation density ρ is extracted for four samples using the DXA method. The densities of total dislocations, Shockley partial dislocations, and perfect dislocations are shown in Fig. 4. Due to the higher stacking fault energy (SFE), the chance of stacking fault in Al alloys is lower than that in Cu and Ni. So the order of ρ in the Al−Mg−Si sample is only 10^{16}, which is nearly one order lower compared with Cu and Ni (low SFE) [21,42]. Generally, in addition to the two dislocations of Shockley partial dislocation and perfect dislocation mentioned above, there are also stair-rod dislocations, Hirth dislocations, Frank dislocations, and partial dislocations with most adaptive dislocations. However, the proportion of these dislocations is relatively small, so they are counted together in the total dislocations and not shown in Fig. 4.

By comparing the dislocation density ρ in the four samples, there is a strong correlation between

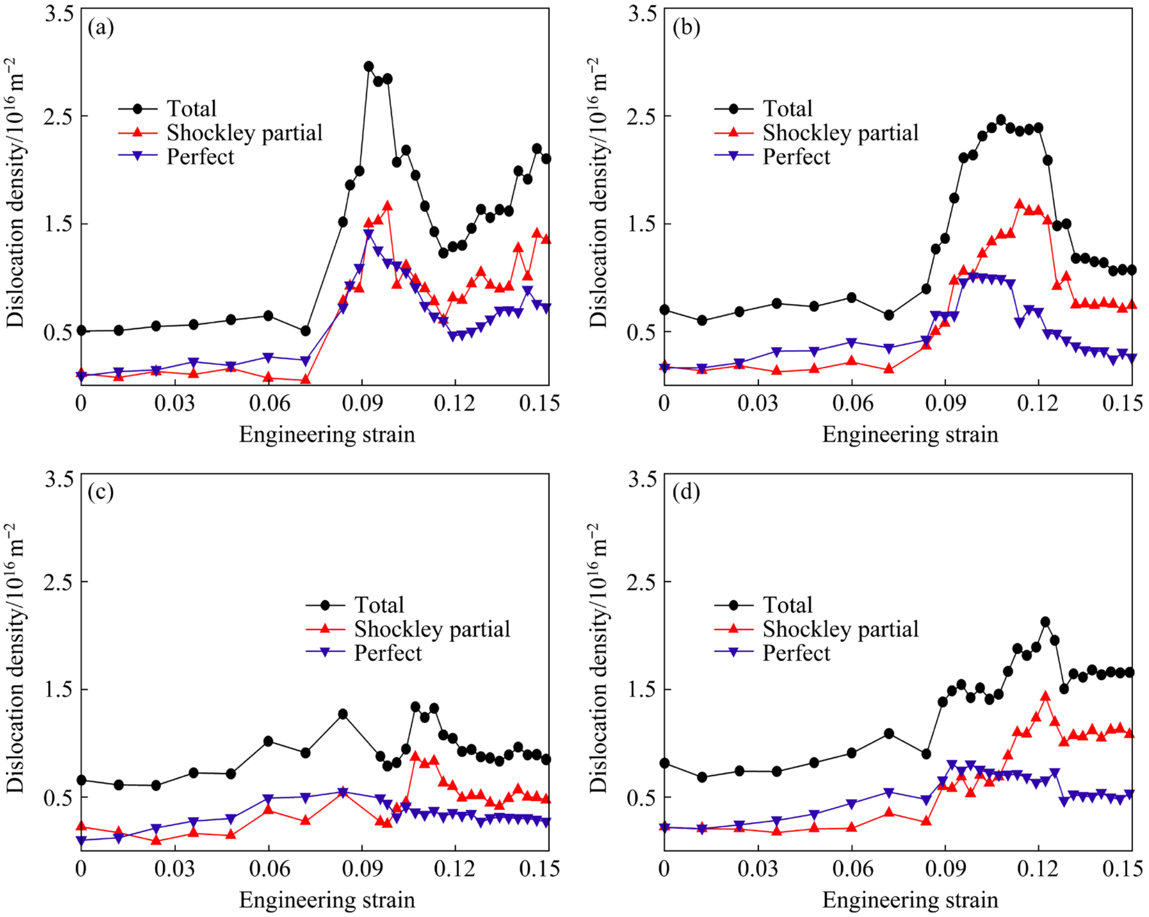

Fig. 4 Dislocation density ρ at φ=0.071 (a), φ=0.107 (b), φ=0.142 (c), and φ=0.178 (d)

the dislocation density and the β'' PVF. Under the same tensile simulation setup and deformation, when φ=0.142, the total dislocation density level is the lowest among the four samples, and its peak value is only 1.3×10^{16} m^{-2}, while the overall level of total dislocation density is much higher at φ=0.107, with a peak of 2.5×10^{16} m^{-2}. At φ=0.178, the φ increases by only 0.036 compared to φ=0.142, while the total dislocation density enhances again immediately, reaching a maximum of 2.1×10^{16} m^{-2}. Dislocation slip is the basic mode of deformation before reaching peak stress for φ=0.107 sample, producing more Shockley partial dislocations and perfect dislocations. But more critically, it can be seen from Figs. 3(b, c) that the local strain of the φ=0.142 sample is more drastic than that of φ=0.107 sample. This may allow the dislocations to act through a deformation mechanism other than annihilation or allowing dislocation to slip, resulting in a lower dislocation density. According to strength $\sigma \propto \rho^{1/2}$ in Ref. [43], it is consistent with the qualitative relationship between the peak stress and the peak total dislocation density in this study.

3.2 Temperature effect on nanomechanical properties of Al−Mg−Si sample with β'' phase

Figure 5(a) shows the engineering stress−strain curves of sample with φ=0.107 at temperatures ranging from 300 to 27 K. The trend of engineering stress−strain curves at different temperatures is similar to that shown in Fig. 2(a) (both rise and fall near a certain mean value after reaching the peak stress). In Fig. 5(b), the peak stress increases steadily upon decreasing temperature. The peak stress is enhanced by 23.35% with 273 K decline in the temperature. The flow stress grows steeply when the temperature reaches 77 K. On contrary, the flow stress shows a gradual increase from 300 to 127 K. The rise in flow stress is 137.43% over the whole temperature range. In conclusion, both peak and flow stresses increase with low temperature, so the cryogenic environments help to improve the strength of the samples during tensile deformation. The temperature effect has also been found in several metals via experiments [44−46].

Figures 5(c, d) give the atomic von Mises

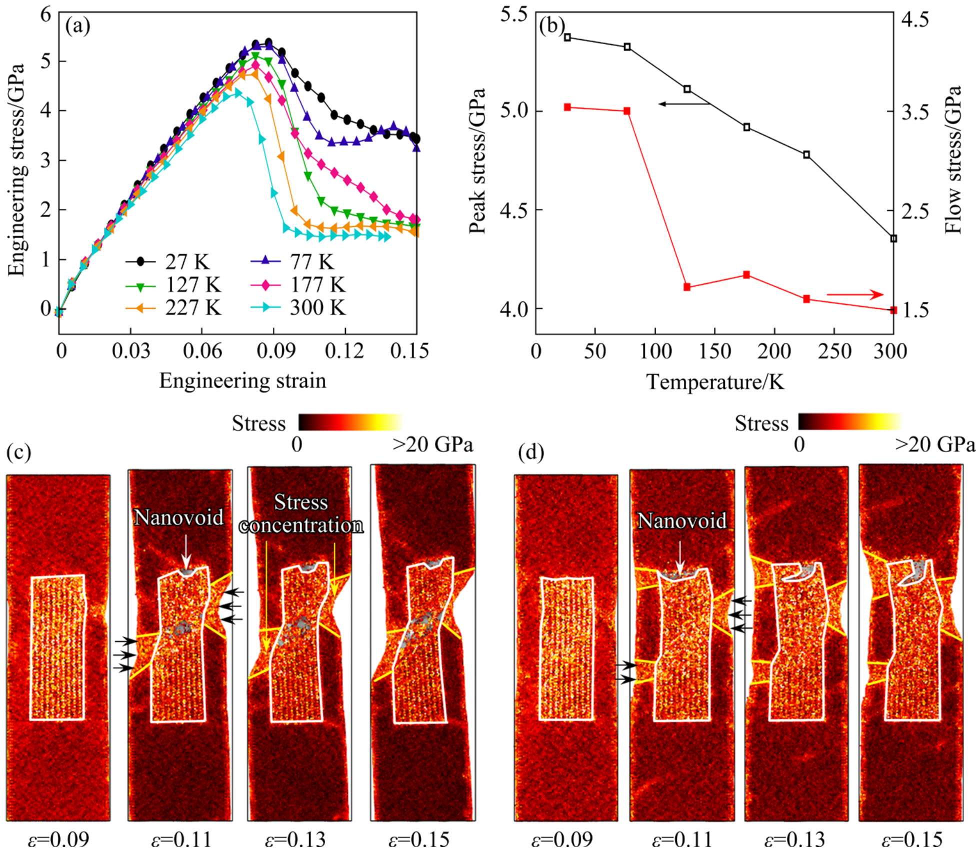

Fig. 5 Nanomechanical properties of sample (φ=0.107) at different temperatures: (a) Engineering stress−strain curves; (b) Peak stress and flow stress vs temperature; (c) Distribution of atomic von Mises stress at 127 K; (d) Distribution of atomic von Mises stress distribution at 177 K

stress ($\sigma_{\text{Mises}}^{\text{Atomic}}$) distribution for samples with deformation temperatures of 127 K and 177 K. The equation is given by

$$\sigma_{\text{Mises}}^{\text{Atomic}}=\{1/2[(\sigma_{xx}-\sigma_{yy})^2+(\sigma_{xx}-\sigma_{zz})^2+(\sigma_{yy}-\sigma_{zz})^2+6(\tau_{xy}^2+\tau_{xz}^2+\tau_{yz}^2)]\}^{1/2} \tag{4}$$

where σ and τ denote the principal stress and shear stress to which individual atoms are subjected, respectively. For both samples stretched at 127 and 177 K, the higher von Mises stress is mainly concentrated inside the β'' phase, and the stress distribution in the Al matrix is lower and relatively uniform. In Figs. 5(c, d), as the engineering strain ε increases from 0.11 to 0.15, nanovoids start to appear at the top and middle of the Al/β'' interface, and the void volume fraction (VVF, φ_{V}) increases continuously at 127 and 177 K (Fig. 6(a)). In addition, it can be seen from Figs. 5(c, d) that the von Mises stress in the Al matrix decreases after the appearance of nanovoids (the color of the Al matrix becomes darker). Some Al atoms close to the β'' phase contract inward because the necking occurs in the waist of the samples (marked with black arrows). Also, their motions are blocked by the β'' phase, and thus stress concentration (marked with yellow lines) appears in some localities in the middle of the samples.

Figure 6(a) gives the evolution curves of VVF−strain at different tensile temperatures. These curves evolve in various ways at different temperatures, so they can be roughly divided into three groups. The curves of samples at 27 and 77 K are the first group, with the lower overall VVF throughout the deformation. With the middle level of VVF in all samples, the curves of samples at 127 and 177 K are the second group. And the curves of samples at 227 and 300 K are the third group, which show the earlier growth point and the faster growth rate of VVF among the three groups. Figure 6(b) shows the local enlargement of the sample at 227 K, which gives both the atomic strain distribution and the evolution of the nanovoid regions. The light gray free surface represents the boundary in the x-direction to show the necking phenomenon, so it can be seen that the larger the engineering strain ε is, the more the sample shrinks inward. The nanovoids encircled by the dark gray surface are surrounded by atoms of higher atomic strain (along the y-axis). It is also evident that the strains of the atoms in the necking region are generally higher than those in other regions. At ε=0.09, shear bands of 45° and 135° start to form on the left and right sides of the sample. As the engineering strain increases, ε goes from 0.11 to 0.15, and these two shear bands are unable to propagate to the interior of the β'' phase. In other words, the β'' phase enhances the ability to resist deformation, and this benefit is reinforced by the temperature effect. This is why the mechanical properties of the sample are better at cryogenic temperatures. The takeaway for us is that cryogenic temperatures can lead to a more efficient strengthening in Al−Mg−Si alloys.

Microscopically, the ductile fracture (DF) behavior occurs as a holistic process of nanovoid-nucleation, nanovoid-growth, and nanovoid-coalescence, which is related to the micro-mechanism of temperature effect. According to Ref. [47], the critical strain (ε_{n}) to nucleate nanovoids

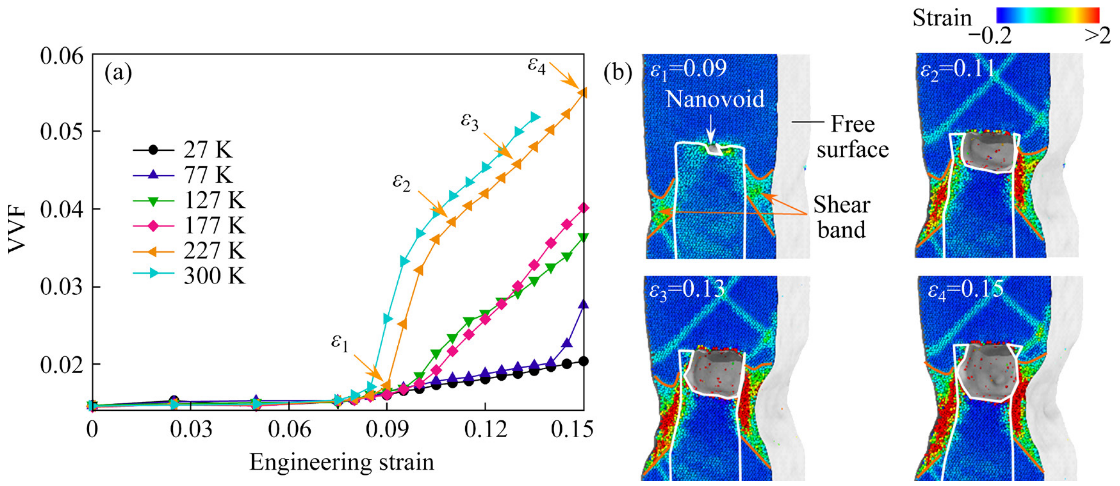

Fig. 6 Effect of temperature on VVF (a) and distribution of atomic strain, and evolution of nanovoids at 227 K (b)

of the VVF−strain curve (Fig. 6(a)) is defined as the nucleation point of nanovoid. In all cases of temperature, $\varepsilon_n\approx0.075$. Meanwhile, damage accumulation is evaluated using nanovoid-growth rate (D_g):

$$D_g=(\varphi_{v,f}-\varphi_{v,n})/(t_f-t_n) \tag{5}$$

where $\varphi_{v,f}$ and t_f are the final VVF and time, $\varphi_{v,n}$ and t_n are the critical VVF and time to nucleate nanovoids. Here the D_g is considered as the main index of DF criterion, and then the lower the D_g is, the better the ductility is. When the temperature is 300 K, D_g is 6.1×10^{-4} ps^{-1}; D_g decreases to 5.3×10^{-4} ps^{-1} for 227 K, and D_g is 1.6×10^{-4} ps^{-1} for 77 K; while temperature is 27 K, D_g is 7×10^{-5} ps^{-1} (decreasing by 88.5% compared to 300 K). So, the reduced temperature enhances the ductility of Al−Mg−Si alloys at cryogenic temperatures.

To characterize the effect of temperature on the dislocation activity of Al−Mg−Si alloys, the dislocation density ρ was also extracted and counted using the DXA method, as shown in Fig. 4. The density of total dislocation, Shockley partial dislocation, and perfect dislocation at different temperatures are shown in Fig. 7. It is directly shown that the cryogenic environment can promote the growth of dislocation, thus improving the effect of dislocation strengthening. In Fig. 7(a), the total dislocation density at 27 K starts to increase at the engineering strain ε of 0.064, while the dislocation densities at other temperatures show a steep increase only at ε larger than 0.08.

Upon decreasing temperature from 300 to 27 K, the peaks of total dislocation density are 1.3×10^{16}, 1.8×10^{16}, 2.0×10^{16}, 1.7×10^{16}, 2.5×10^{16}, and 3.2×10^{16} m^{-2}, respectively, and the overall peak of total dislocation density is increased by about 146% with the temperature declining. At the lower temperature of 77 K, dislocation annihilation rarely takes place, thereby increasing the dislocation density [48]. In addition, by comparing Fig. 7(b) with 7(c), it is found that the overall level of Shockley partial dislocation density can be higher than that of perfect dislocation density throughout the stretching. Meanwhile, the observation reveals that the lower the temperature is, the more favorable the growth of Shockley partial dislocation is, with an increase of 83.61% at 27 K, which means that more stacking faults are generated in the sample.

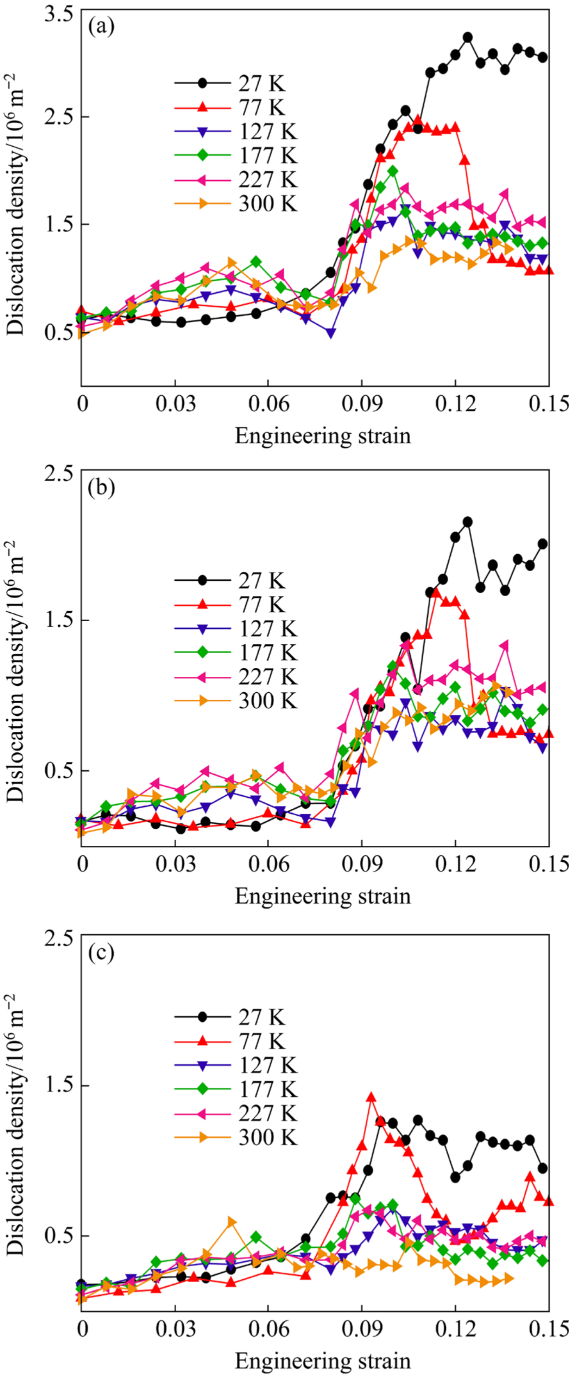

Fig. 7 Evolution of dislocation density ρ at cryogenic temperatures: (a) Total dislocation; (b) Shockley partial dislocation; (c) Perfect dislocation

4 Conclusions

(1) For the y-axis uniaxial tensile test of the samples, the flow stress and the peak stress reach the maximum when the β'' phase volume fraction (PVF, φ) is 0.107. Compared to peak stress of pure aluminum, the peak stress of Al−Mg−Si alloy sample with β'' PVF of 0.107 is increased by 97.05%.

(2) With decreasing the temperature from 300 to 27 K, both the peak stress and ductility of the sample with β'' PVF of 0.107 increase. The peak stress is increased by 23.35% from 4.4 GPa at 300 K to 5.4 GPa at 27 K. And the lower the temperature is, the more difficultly the top of the Al/β'' interface is torn, and the smaller the resulting void volume fraction and nanovoid-growth rate are (decreased by up to 88.5%).

(3) The von Mises stress distribution suggests that the high-stress region is more concentrated in the β'' phase. Furthermore, the trend of the peak total dislocation density increases at a lower temperature. Thus, cryogenic temperatures can contribute to the overall improvement of the nanomechanical properties of Al−Mg−Si alloys.

Acknowledgments

This work was supported by the High Performance Computing Center of Central South University, China, the High-tech Industry Technology Innovation Leading Plan of Hunan Province, China (No. 2020GK2032), the National Natural Science Foundation of China (No. 52105419), and the Research Fund of the Key Laboratory of High Performance Complex Manufacturing at Central South University, China.

References

[1] HIRSCH J, AL-SAMMAN T. Superior light metals by texture engineering: Optimized aluminum and magnesium alloys for automotive applications [J]. Acta Materialia, 2013, 61: 818−843.

[2] WENG Yao-yao, JIA Zhi-hong, DING Li-peng, LIAO Jin, ZHANG Ping-ping, XU Ya-qi, LIU Qing. Effect of pre-straining on structure and formation mechanism of precipitates in Al−Mg−Si−Cu alloy [J]. Transactions of Nonferrous Metals Society of China, 2022, 32: 436−447.

[3] WANG Lin, BHATTA L, XIONG Han-qing, LI Chang, CUI Xiao-hui, KONG C, YU Hai-liang. Mechanical properties and microstructure evolution of an Al−Cu−Li alloy subjected to rolling and aging [J]. Journal of Central South University, 2021, 28: 3800−3817.

[4] ANDERSEN S J, ZANDBERGEN H W, JANSEN J, TRÆHOLT C, TUNDAL U, REISO O. The crystal structure of the β'' phase in Al−Mg−Si alloys [J]. Acta Materialia, 1998, 46: 3283−3298.

[5] SHA G, MÖLLER H, STUMPF W E, XIA J H, GOVENDER G, RINGER S P. Solute nanostructures and their strengthening effects in Al−7Si−0.6Mg alloy F357 [J]. Acta Materialia, 2012, 60(2): 692−701.

[6] WANG Xiang-dong, LIU Xiong, DING Hao, YAN Su-rong, XIE Zi-hua, PAN Bai-qing, LI Yong-hong, PAN Qing-lin, DENG Yun-lai, WANG Wei-yi. Microstructure and mechanical properties of Al−Mg−Si alloy U-shaped profile [J]. Transactions of Nonferrous Metals Society of China, 2020, 30(11): 2915−2926.

[7] NANDY S, KUMAR R K, DAS D. Process model to predict yield strength of AA6063 alloy [J]. Materials Science and Engineering A, 2015, 644: 413−424.

[8] TAKAHASHI Y, KURIKI R, KURIHARA J, KOZAWA T, SHIKAMA T, NOGUCHI H. Distinct fatigue limit of a 6XXX series aluminum alloy in relation to crack tip strain-aging [J]. Materials Science and Engineering A, 2020, 785: 139378.

[9] ANDERSEN S J, MARIOARA C D, FRØSETH A, VISSERS R, ZANDBERGEN H W. Crystal structure of the orthorhombic U2-$Al_4Mg_4Si_4$ precipitate in the Al−Mg−Si alloy system and its relation to the β' and β'' phases [J]. Materials Science and Engineering A, 2005, 390: 127−138.

[10] WU Ge, LIU Chang, SUN Li-gang, WANG Qing, SUN Bao-an, HAN Bin, KAI Ji-jung, LUAN Jun-hua, LIU C T, CAO Ke, LU Yang, CHENG Li-zi, LU Jian. Hierarchical nanostructured aluminum alloy with ultrahigh strength and large plasticity [J]. Nature Communications, 2019, 10: 5099.

[11] GOLOVASHCHENKO S, REINBERG N, WANG N, LE Q. Effect of material structure on trimming and sheared edge stretchability of 6xxx aluminum alloys [J]. IOP Conference Series: Materials Science and Engineering, 2019, 651: 012027.

[12] PANIGRAHI S K, JAYAGANTHAN R. Effect of rolling temperature on microstructure and mechanical properties of 6063 Al alloy [J]. Materials Science and Engineering A, 2008, 492: 300−305.

[13] PANIGRAHI S K, JAYAGANTHAN R, PANCHOLI V. Effect of plastic deformation conditions on microstructural characteristics and mechanical properties of Al 6063 alloy [J]. Materials & Design, 2009, 30: 1894−1901.

[14] YU Hai-liang, LU Cheng, TIEU K, LIU Xiang-hua, SUN Yong, YU Qing-bo, KONG C. Asymmetric cryorolling for fabrication of nanostructural aluminum sheets [J]. Scientific Reports, 2012, 2: 772.

[15] NAGESWARA R P, JAYAGANTHAN R. Effects of warm rolling and ageing after cryogenic rolling on mechanical properties and microstructure of Al 6061 alloy [J]. Materials & Design, 2012, 39: 226−233.

[16] LIU Yue, ZHAO Xiang-shuai, LI Jing, BHATTA L, LUO Kai-guang, KONG C, YU Hai-liang. Mechanical properties of rolled and aged AA6061 sheets at room-temperature and cryogenic environments [J]. Journal of Alloys and Compounds, 2021, 860: 158449.

[17] GOLOVASHCHENKO S, WANG N, LE Q. Trimming and sheared edge stretchability of automotive 6xxx aluminum alloys [J]. Journal of Materials Processing Technology, 2019, 264: 64−75.

[18] LEE Woei-shyan, HUANG Yu-chi. Mechanical properties and dislocation substructure of 6061-T6 aluminum alloy impacted at cryogenic temperatures [J]. Materials Transactions, 2016, 57: 344−350.

[19] YUAN Lin, SHAN De-bin, GUO Bin. Molecular dynamics simulation of tensile deformation of nano-single crystal aluminum [J]. Journal of Materials Processing Technology, 2007, 184: 1−5.

[20] ZEPEDA-RUIZ L A, STUKOWSKI A, OPPELSTRUP T, BULATOV V V. Probing the limits of metal plasticity with molecular dynamics simulations [J]. Nature, 2017, 550(7677): 492−495.

[21] KO W S, STUKOWSKI A, HADIAN R, NEMATOLLAHI A, JEON J B, CHOI W S, DEHM G, NEUGEBAUER J, KIRCHLECHNER C, GRABOWSKI B. Atomistic deformation behavior of single and twin crystalline Cu nanopillars with preexisting dislocations [J]. Acta Materialia, 2020, 197: 54−68.

[22] DENG Xiao-zhen, LANG Lin, MO Yun-fei, DONG Ke-jun, TIAN Ze-an, HU Wang-yu. Solid−solid phase transition of tungsten induced by high pressure: A molecular dynamics simulation [J]. Transactions of Nonferrous Metals Society of China, 2020, 30(11): 2980−2993.

[23] ZANDBERGEN H W, ANDERSEN S J, JANSEN J. Structure determination of Mg_5Si_6 particles in Al by dynamic electron diffraction studies [J]. Science, 1997, 277(5330): 1221−1225.

[24] PERSSON K. Materials data on Mg_5Si_6 (SG: 12) by materials project [EB/OL]. 2016, https://materialsproject.org/materials/mp-31404/#.

[25] RAVI C, WOLVERTON C. First-principles study of crystal structure and stability of Al−Mg−Si−(Cu) precipitates [J]. Acta Materialia, 2004, 52: 4213−4227.

[26] EHLERS F J H, DUMOULIN S, HOLMESTAD R. 3D modelling of β'' in Al–Mg–Si: Towards an atomistic level *ab initio* based examination of a full precipitate enclosed in a host lattice [J]. Computational Materials Science, 2014, 91: 200−210.

[27] EHLERS F J H, DUMOULIN S. Interface configuration stability and interfacial energy for the β'' phase in Al–Mg–Si as examined with a first principles based hierarchical multi-scale scheme [J]. Journal of Alloys and Compounds, 2014, 591: 329−336.

[28] JELINEK B, GROH S, HORSTEMEYER M F, HOUZE J, KIM S G, WAGNER G J, MOITRA A, BASKES M I. Modified embedded atom method potential for Al, Si, Mg, Cu, and Fe alloys [J]. Physical Review B, 2012, 85(24): 245102.

[29] XIAO Shi-di, KONG Yi, QIU Yue, DU Yong. The microstructure evolution of U1 and U2 nanowires constrained in Al matrix [J]. Computational Materials Science, 2016, 117: 180−187.

[30] QIU Yue, KONG Yi, XIAO Shi-di, DU Yong. Mechanical properties of β'' precipitates containing Al and/or Cu in age hardening Al alloys [J]. Journal of Materials Research, 2016, 31(5): 580−588.

[31] LIAO M, LI B, HORSTEMEYER M F. Interaction between prismatic slip and a $Mg_{17}Al_{12}$ precipitate in magnesium [J]. Computational Materials Science, 2013, 79: 534−539.

[32] LIAO M, LI B, HORSTEMEYER M F. Interaction between basal slip and a $Mg_{17}Al_{12}$ precipitate in magnesium [J]. Metallurgical and Materials Transactions A, 2014, 45: 3661−3669.

[33] VAID A, GUÉNOLÉ J, PRAKASH A, KORTE-KERZEL S, BITZEK E. Atomistic simulations of basal dislocations in Mg interacting with $Mg_{17}Al_{12}$ precipitates [J]. Materialia, 2019, 7: 100355.

[34] MARIOARA C D, ANDERSEN S J, ZANDBERGEN H W, HOLMESTAD R. The influence of alloy composition on precipitates of the Al−Mg−Si system [J]. Metallurgical and Materials Transactions A, 2005, 36: 691−702.

[35] PLIMPTON S. Fast parallel algorithms for short-range molecular dynamics [J]. Journal of Computational Physics, 1995, 117(1): 1−19.

[36] STUKOWSKI A. Visualization and analysis of atomistic simulation data with OVITO–the Open Visualization Tool [J]. Modelling and Simulation in Materials Science and Engineering, 2010, 18(1): 015012.

[37] STUKOWSKI A, ALBE K. Extracting dislocations and non-dislocation crystal defects from atomistic simulation data [J]. Modelling and Simulation in Materials Science and Engineering, 2010, 18(8): 085001.

[38] STUKOWSKI A, BULATOV V V, ARSENLIS A. Automated identification and indexing of dislocations in crystal interfaces [J]. Modelling and Simulation in Materials Science and Engineering, 2012, 20(8): 085007.

[39] CHOI Won-mi, JO Yong-hee, SOHN Seok-su, LEE Sunghak, LEE Byeong-joo. Understanding the physical metallurgy of the CoCrFeMnNi high-entropy alloy: An atomistic simulation study [J]. npj Computational Materials, 2018, 4: 1.

[40] CHENG Y Q, CAO A J, MA E. Correlation between the elastic modulus and the intrinsic plastic behavior of metallic glasses: The roles of atomic configuration and alloy composition [J]. Acta Materialia, 2009, 57: 3253−3267.

[41] DING Yu, YU Hai-yang, ZHAO Kai, LIN Mei-chao, XIAO Sen-bo, ORTIZ M, HE Jian-ying, ZHANG Zhi-liang. Hydrogen-induced transgranular to intergranular fracture transition in bi-crystalline nickel [J]. Scripta Materialia, 2021, 204: 114122.

[42] WANG Yao-dong, LI Jian-jun, LU Wen-jun, YUAN Fu-ping, WU Xiao-lei. Enhanced co-deformation of a heterogeneous nanolayered Cu/Ni composite [J]. Journal of Applied Physics, 2019, 126(21): 215111.

[43] KAMIKAWA N, HUANG X X, TSUJI N, HANSEN N. Strengthening mechanisms in nanostructured high-purity aluminium deformed to high strain and annealed [J]. Acta Materialia, 2009, 57: 4198−4208.

[44] KOTRECHKO S, OVSJANNIKOV A. Temperature dependence of the yield stress of metallic nano-sized crystals [J]. Philosophical Magazine, 2009, 89(33): 3049−3058.

[45] KOTRECHKO S, OVSJANNIKOV O, STETSENKO N, MIKHAILOVSKIJ I, MAZILOVA T, STAROSTENKOV M. Yield strength temperature dependence of tungsten nanosized crystals: Experiment and simulation [J]. Philosophical Magazine, 2016, 96(5): 473−485.

[46] HUANG Ke, HUANG Shi-quan, YI You-ping, DONG Fei, HE Hai-lin. Flow behavior and forming characteristics of 2A14 aluminum alloy at cryogenic temperatures [J]. Journal of Alloys and Compounds, 2022, 902: 163821.

[47] NIU Li-qun, ZHANG Qi, MA Ying-song, CHEN Yu-jie, HAN Bin, HUANG Ke. A ductile fracture criterion under warm-working conditions based on the multiscale model combining molecular dynamics with finite element methods [J]. International Journal of Plasticity, 2022, 149: 103185.

[48] PAL S, BABU P N, GARGEYA B S K, BECQUART C S. Molecular Dynamics simulation based investigation of possible enhancement in strength and ductility of nanocrystalline aluminum by CNT reinforcement [J]. Materials Chemistry and Physics, 2020, 243: 122593.

含 β''-Mg_5Si_6 相 Al−Mg−Si 合金深冷环境强塑双增原子级机理

雷 刚 [1,2]，高海涛 [1,2,3]，张 昀 [1,2]，崔晓辉 [1,2,3]，喻海良 [1,2,3]

1. 中南大学 机电工程学院，长沙 410083；
2. 中南大学 极端服役性能精准制造全国重点实验室，长沙 410083；
3. 中南大学 轻合金研究院，长沙 410083

摘 要：采用分子动力学方法研究 β''-Mg_5Si_6 析出相体积分数及深冷温度对 Al−Mg−Si 合金纳米力学特性的影响。模拟结果表明，与纯 Al 的峰值应力相比，当温度为 77 K、β''析出相体积分数为 0.107 时，Al−Mg−Si 合金的峰值应力提高 97.05%。当 β''析出相体积分数为 0.107 时，与 300 K 下样品的峰值应力相比，在 27 K 下该样品的峰值应力可提高 23.55%。研究结果表明，深冷环境有助于提高总位错密度，使样品能够承受更大的应力，这为含 β'' 相的 Al−Mg−Si 合金提供额外强度和韧性。降低温度可以明显抑制孔洞的萌生和生长(生长率 27 K 时下降 88.5%)，从而提高 Al−Mg−Si 合金的塑性。

关键词：分子动力学；铝合金；β''相；强度；韧性；深冷温度

(Edited by Bing YANG)